Non-equilibrium characteristics analysis of argon inductively coupled plasma*

Zhang Hui[1], Han Ning[1], Meng Xian[1, *], Cao Jinwen[1, 2], Sun Wenjin[1, 2], Li Mengtian[1, 2], Geng Jinyue[1], Huang Heji[1, 2]

1. State Key Laboratory of High-Temperature Gas Dynamics, Institute of Mechanics, Chinese Academy of Sciences, Beijing 100190
2. School of Engineering Science, University of Chinese Academy of Sciences, Beijing 100049

Abstract
Inductively coupled plasma (ICP) generators involve complex interactions between electromagnetic, thermal, and chemical processes, which makes direct diagnostics difficult. To clarify these coupling mechanisms, a two-dimensional axisymmetric model of an argon ICP torch operating at kilopascal pressure is implemented in COMSOL Multiphysics under local thermodynamic equilibrium (LTE) and non-equilibrium (NLTE) assumptions. A two-dimensional axisymmetric magnetohydrodynamic (MHD) model is established, which combines electromagnetic induction, convective-radiative heat transfer, and a seven-reaction argon plasma chemistry mechanism. The LTE model assumes that the temperature of all species is uniform, while the NLTE model independently solves for the electron temperature (T_e) and gas temperature (T_g), thereby accounting for incomplete energy exchange between electrons and heavy particles. At a discharge power of 1000 W and a working pressure of 10 kPa, the LTE model predicts a peak temperature of approximately 8200 K, concentrated around the induction coils. In contrast, the NLTE model yields a maximum gas temperature of about 5990 K, with the hot zone shifted downstream. The NLTE model reveals a pronounced two-temperature structure: T_e peaks near the coil wall (~0.93 eV), while T_g reaches its maximum downstream, indicating a pronounced thermal non-equilibrium state where electrons are preferentially heated

* The paper is an English translated version of the original Chinese paper published in Acta Physica Sinica. Please cite the paper as: Zhang Hui[1], Han Ning[1], Meng Xian[1, *], Cao Jinwen[1, 2], Sun Wenjin[1, 2], Li Mengtian[1, 2], Geng Jinyue[1], Huang Heji[1, 2], **Non-equilibrium characteristics analysis of argon inductively coupled plasma** . *Acta Phys. Sin.*, 2025, 74(23):235215. doi: 10.7498/aps.74.20251186

by the induced field. The calculated skin depth (~11.3 mm) coincides with the region of strongest electromagnetic energy deposition. Species analysis shows that the plasma core is dominated by ground-state argon (Ar) (>99%), while excited argon (Ar*) and argon ions (Ar^+) increase notably near the coil region, confirming that excitation and ionization processes are localized within the skin layer. Furthermore, comparison between the 5 kPa and 10 kPa cases shows that as pressure decreases, the difference between T_e and T_g increases, indicating enhanced thermal non-equilibrium due to reduced collisional coupling. Overall, the results highlight that LTE and NLTE assumptions lead to markedly different predictions of temperature and energy coupling at kilopascal pressures. The NLTE model more realistically captures delayed energy transfer and spatial temperature decoupling, offering new insights into the electromagnetic-thermal-flow interactions of ICP discharges and providing a modeling reference for designing ICP-based high-enthalpy plasma wind tunnel and realizing related aerospace applications.

Keywords: inductively coupled plasma; argon plasma; non-equilibrium characteristics;

PACS:52.50.Dg; 52.25.Kn; 52.50.Qt; 52.65.-y

DOI: 10.7498/aps.74.20251186

cstr: 32037.14.aps.74.20251186

1 Introduction

Hypersonic vehicles operating in near-space environments encounter severe challenges in accurately predicting aerodynamic heating due to high-temperature real-gas effects and thermochemical nonequilibrium during prolonged flight. Inductively coupled plasma (ICP) wind tunnels, characterized by electrodeless discharge, avoid electrode contamination[1] and thus provide a cleaner ground-test environment for investigating such complex flows. Extensive research has been conducted globally in this domain. The von Karman Institute for Fluid Dynamics (VKI) developed an inductively coupled wind tunnel (plasmatron)[2,3] capable of simulating aerothermal conditions during planetary atmospheric entry. The Japan Aerospace Exploration Agency (JAXA) established a 110 kW high-frequency plasma wind tunnel[4] to study argon plasma discharges. The Institute of Mechanics, Chinese Academy of Sciences[5] investigated surface catalytic properties of materials using a 30 kW high-frequency wind tunnel. Furthermore, the China Aerodynamics Research and Development Center operates a 1 MW high-frequency plasma wind tunnel[6,7] for experimental studies on surface catalysis, oxidation, and radiative characteristics of thermal protection materials for aerospace vehicles.

Experimental and numerical studies have demonstrated that, during actual ICP discharges, certain regions fail to satisfy local thermodynamic equilibrium (LTE) conditions[8]. Specifically, the electron temperature (T_e) exceeds the heavy-particle temperature (T_h), indicating a state of non-local thermodynamic equilibrium (NLTE). These nonequilibrium regions predominantly occur at the periphery of the plasma jet, particularly near the quartz tube within the coil coverage area[9,10].

Operating pressure critically determines the thermodynamic state of the plasma. Under high-pressure conditions, frequent interparticle collisions ensure LTE within the plasma torch, allowing electron temperature (T_e), heavy-particle temperature (T_h), and excitation temperature to be represented by a single temperature parameter T. Consequently, equilibrium discharge models are typically employed for high-pressure ICP simulations. In contrast, at low pressures, reduced collision frequency diminishes energy transfer efficiency between electrons and heavy particles, resulting in $T_e \neq T_h$. Under such conditions, nonequilibrium models are essential for accurately describing plasma behavior.

Accurate experimental measurement of plasma parameters remains challenging due to the extreme temperatures, confined spatial dimensions within the ICP torch, and the coupled effects of electromagnetic fields and complex high-temperature chemical reactions. Therefore, numerical simulation has become a vital approach for studying discharge and flow characteristics[11-16]. In low-pressure nonequilibrium plasma simulations, Stewart et al.[17] examined spatial distributions of plasma density and electron temperature in argon ICP discharges within the 1-20 mTorr range (1 Torr = 133 Pa). Lei et al.[18] employed COMSOL to simulate argon ICP nonequilibrium discharges at 2-10 Pa, obtaining spatial distributions of flow-field parameters under varying input power and pressure settings. Regarding equilibrium plasma studies, Punjabi et al.[19] used Fluent to analyze the influence of different gas discharges at atmospheric pressure on temperature and velocity fields under thermodynamic equilibrium. Zhu et al.[20] developed a three-dimensional radio-frequency thermal plasma model incorporating the actual solenoid structure of the induction coil to compute distributions of temperature, flow, and electromagnetic fields. Yu et al.[21] simulated argon discharges in a segmented atmospheric-pressure ICP torch using COMSOL, obtaining temperature and flow-field distributions under equilibrium conditions and elucidating the underlying physical mechanisms. Collectively, these studies have elucidated discharge characteristics, flow structures, and intrinsic physical mechanisms of ICP plasmas across diverse operating conditions-from low-pressure nonequilibrium to high-pressure equilibrium regimes.

In high-enthalpy plasma wind tunnels, ICP torches are often integrated with nozzles to generate high-speed jets or enable propulsion applications. Under the combined effects of upstream gas supply and nozzle throat dynamics, the discharge chamber pressure can be maintained in the kilopascal range[4,22]. Although significant progress has been made in ICP numerical simulations, systematic investigations in the kilopascal pressure regime remain limited. Accordingly, this study focuses on an operating pressure of 10 kPa and establishes a two-dimensional axisymmetric numerical model of an ICP torch. Using COMSOL, we simulate argon discharge processes and systematically compare thermal characteristics of the ICP flow field under equilibrium and nonequilibrium models. This analysis elucidates discrepancies in energy distribution and temperature field evolution arising from different modeling approaches at kilopascal pressures, thereby offering new insights into the applicability and limitations of ICP simulation methodologies within this pressure regime.

2 ICP Magnetohydrodynamic Model

In the LTE model, the energy distributions of all plasma species-electrons, ions, and neutral atoms-are assumed to be characterized by a single temperature T, that is,

$$T_{\mathrm{e}} = T_{\mathrm{h}} = T_{\mathrm{v}} = T_{\mathrm{r}} = T \tag{1}$$

Here, T_{e}, T_{h}, T_{v}, and T_{r} denote the electron, heavy-particle, vibrational, and rotational temperatures, respectively. For monatomic gases, only the electron temperature T_{e} and heavy-particle temperature T_{h} exist. Under this model, energy exchange is assumed to be fully coupled, and local thermodynamic equilibrium prevails between electrons and heavy particles. The governing equations are solved by coupling electromagnetic and hydrodynamic equations through a magnetohydrodynamic (MHD) approach to obtain the flow and temperature fields (see Sections 2.1-2.2 for the computational equations).

In the non-local thermodynamic equilibrium (NLTE) model, the finite rate of energy exchange between electrons and heavy particles is explicitly considered, and the electron temperature T_{e} and gas temperature T are solved independently:

$$T_{\mathrm{e}} \neq T_{\mathrm{h}} \approx T \tag{2}$$

The NLTE model captures the effects of incomplete energy exchange between electrons and heavy particles. It separately formulates an electron energy equation and a gas energy equation, while additionally incorporating models for electron and ion dynamics as well as chemical reaction kinetics (see Sections 2.1-2.4 for the governing equations).

2.1 Electromagnetic Field Equations

Under the fundamental assumptions that the plasma is quasi-neutral and displacement current is negligible, Maxwell's equations take the following form:

$$\nabla \times \boldsymbol{E} = -\frac{\partial \boldsymbol{B}}{\partial t} \quad (3)$$

$$\nabla \times \boldsymbol{B} = \mu(\boldsymbol{J}_{\mathrm{coil}} + \boldsymbol{J}_{\mathrm{p}}) + \varepsilon\mu\frac{\partial \boldsymbol{E}}{\partial t} \quad (4)$$

$$\nabla \cdot \boldsymbol{D} = \rho \quad (5)$$

$$\nabla \cdot \boldsymbol{B} = 0 \quad (6)$$

Here, *is developed using COMSOL Multiphysics* = $\mu_0\mu_r$ denotes magnetic permeability, $\varepsilon = \varepsilon_0\varepsilon_r$ represents permittivity, $\boldsymbol{J}_p$ indicates the induced current density in the plasma, $\boldsymbol{J}_{coil}$ denotes the current density in the coil, and ρ signifies the space charge density.

By introducing the magnetic vector potential $\boldsymbol{A}$, where $\boldsymbol{B} = \nabla \times \boldsymbol{A}$, and substituting into Equation (4), we obtain:

$$(\mathrm{j}\omega\sigma - \omega^2\varepsilon)\boldsymbol{A} + \nabla \times (\frac{1}{\mu}\nabla \times \boldsymbol{A}) = \boldsymbol{J}_{\mathrm{coil}} \quad (7)$$

In the equation, j denotes the imaginary unit, ω represents angular frequency, and σ signifies electrical conductivity.

2.2 Hydrodynamic Equations

For a quasi-neutral gas, the hydrodynamic system comprises the following continuity, momentum, and energy equations:

$$\nabla(\rho u) = 0 \quad (8)$$

$$\nabla(\rho \boldsymbol{u}\boldsymbol{u}) = -\nabla p + \nabla[\mu(\nabla \boldsymbol{u} + (\nabla \boldsymbol{u})^{\mathrm{T}}) - \frac{2}{3}\mu(\nabla \cdot \boldsymbol{u}I)] + (\rho \boldsymbol{g} + \boldsymbol{j} \times \boldsymbol{B}) \quad (9)$$

$$\rho C_{\mathrm{p}}(\frac{\partial T}{\partial t} + \boldsymbol{u} \cdot \nabla T) = \nabla \cdot (k\nabla T) + P_{\mathrm{j}} - Q_{\mathrm{r}} \quad (10)$$

where ρ denotes gas density, p pressure, μ viscosity, T temperature, $\boldsymbol{I}$ the identity matrix, g gravitational acceleration, B magnetic flux density, $\boldsymbol{j}$ induced current density,

C_p specific heat capacity at constant pressure, k thermal conductivity, P_j Joule heating, and Q_r volumetric radiative loss.

For non-equilibrium models, additional considerations include electron and ion dynamics as well as chemical reaction kinetics. Consequently, the following system of equations are additionally required.

2.3 Electron and Ion Equations

$$\frac{\partial}{\partial t}(n_e) + \nabla \cdot \boldsymbol{\Gamma}_e = R_e - (u \cdot \nabla) n_e \tag{11}$$

$$\frac{\partial}{\partial t}(n_i) + \nabla \cdot \boldsymbol{\Gamma}_i = R_i - (u \cdot \nabla) n_i \tag{12}$$

$$\boldsymbol{\Gamma}_e = -n_e(\mu_e \cdot E) - D_e \cdot \nabla n_e \tag{13}$$

$$\boldsymbol{\Gamma}_i = -n_i(\mu_i \cdot E) - D_i \cdot \nabla n_i \tag{14}$$

$$\frac{\partial}{\partial t}(n_\varepsilon) + \nabla \cdot \boldsymbol{\Gamma}_\varepsilon + E \cdot \boldsymbol{\Gamma}_\varepsilon = R_\varepsilon - (\mu_\varepsilon \cdot \nabla) n_\varepsilon \tag{15}$$

Here, n_e and n_i denote the number densities of electrons and ions, respectively; n_ε represents the electron energy density; $\boldsymbol{\Gamma}_e$ and $\boldsymbol{\Gamma}_i$ denote the electron and ion fluxes; $\boldsymbol{\Gamma}_\varepsilon$ denotes the electron energy flux; R_e and R_i represent the electron and ion source terms; R_ε denotes the energy loss due to inelastic collisions; E denotes the electric field; μ_e and μ_i denote the electron and ion mobilities; μ_ε represents the electron energy mobility; D_e and D_i denote the electron and ion diffusion coefficients; and u denotes the neutral fluid velocity. Notably, the velocity u serves as a critical parameter that enables coupling between the flow field and the plasma discharge model[23].

2.4 Chemical Reaction Model

For the selected argon working gas, the model includes argon atoms (Ar), metastable argon atoms (Ar*), argon ions (Ar^+), and electrons (e). The reaction mechanism encompasses seven key chemical processes, including elastic collisions, excitation, and ionization (see Table 1)[18]. These seven reactions collectively describe essential pathways-ranging from ground-state excitation and stepwise ionization to Penning ionization and energy recycling-and accurately capture the generation and evolution of electrons, excited species, and ions in argon inductively coupled plasma (ICP) under the specified pressure conditions. Furthermore, volume reactions with negligible contributions-such as three-body recombination and molecular ion formation-were excluded from this reaction system.

When plasma species collide with the wall, they relax or neutralize to ground-state argon atoms with a certain probability. Accordingly, two surface reactions were also considered: $Ar^* \rightarrow Ar$ and $Ar^+ \rightarrow Ar$, both assigned a sticking coefficient of 1.

Table 1 Argon chemical reactions[18].

反应	反应方程	反应类型	反应速率系数	$\Delta\varepsilon$/eV
1	e + Ar → e + Ar	弹性碰撞	k_{el}	—
2	e + Ar → e + Ar*	激发	k_{ex}	11.56
3	e + Ar* → e + Ar	激发	k_{sc}	–11.56
4	e + Ar → 2e + Ar^+	电离	k_i	15.6
5	e + Ar* → 2e + Ar^+	电离	k_{si}	4.14
6	Ar*+Ar* → e+Ar+Ar^+	潘宁电离	k_{mp}	—
7	Ar + Ar* → Ar + Ar	亚稳猝灭	k_{2p}	—

3 ICP Plasma Torch Model

We employed a two-dimensional axisymmetric geometric model, as illustrated in Figure 1, based on the high-frequency inductively coupled plasma (ICP) generator of the Long-Duration Hypervelocity Rarefied Gas Wind Tunnel at the Institute of Mechanics, Chinese Academy of Sciences. This model comprises several key regions: Region A represents the plasma flow field, Region B denotes the ambient air surrounding the model, Region C corresponds to the circulating cooling water inside the insulating tube, Region D constitutes the insulating tube structure, and the annular Region E represents the coil assembly. Argon served as the working gas in this study. Under equilibrium discharge conditions, the temperature-dependent thermophysical properties of argon were obtained from the fundamental gas discharge plasma database established by Xi'an Jiaotong University[24].

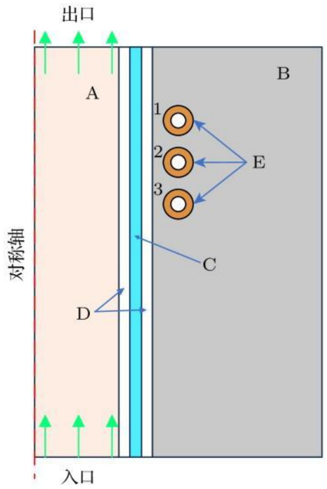

Fig. 1 Schematic diagram of the structure of the inductively coupled plasma generator.

The inductively coupled plasma torch measures 128 mm in height and 42 mm in inner diameter, with a quartz tube wall thickness of 2 mm. The induction coil has a diameter of 8 mm and is positioned between 72 mm - 98 mm from the inlet, spaced at 13 mm intervals. The coil is located 33.5 mm from the central axis of the plasma torch.

The inductively coupled plasma generator adopts a cylindrical structural design, with the gas inlet situated at the bottom. In numerical simulations, the computational domain was extended slightly beyond the generator's physical boundaries. This ensures that the induced magnetic field remains fully contained within the domain and enhances the fidelity of the simulation to actual operating conditions.

Figure 2 illustrates the computational mesh for the inductively coupled plasma generator. To improve numerical stability and convergence, mesh refinement was applied in critical regions. Boundary layer meshing was implemented near the discharge tube wall to accurately resolve plasma-wall interactions and thermal boundary layer characteristics. Additionally, local mesh refinement was performed around the coil region to guarantee precision in electromagnetic field calculations.

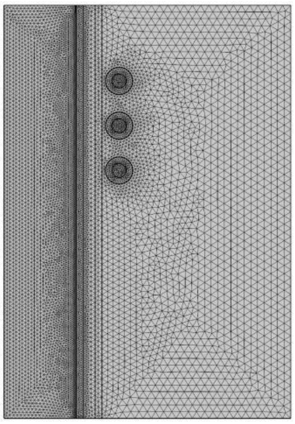

Fig. 2 Meshing of inductively coupled plasma generator.

4 Analysis of Computational Results

In the numerical simulations, the working pressure was set to 10 kPa, the discharge frequency to 13.56 MHz, the inlet mass flow rate to 10 sccm (1 sccm = 1 mL/min at standard atmospheric pressure), the initial plasma temperature to 300 K, and the coil power to 1000 W. Based on this model, we simulated the spatial distribution characteristics and variation patterns of physical parameters in argon inductively coupled plasma.

4.1 Comparison Between Non-Equilibrium and Equilibrium ICP Numerical Simulations

Figure 3 presents temperature contour plots of 1000 W inductively coupled plasma under non-local thermodynamic equilibrium (NLTE) and local thermodynamic equilibrium (LTE) conditions. The results reveal significant differences in both the location and magnitude of the peak gas temperatures. In the LTE model, the temperature maximum occurs near the induction coil, reaching approximately 8200 K. In contrast, the NLTE model shows the peak shifted downstream of the coil, with a maximum temperature of only 5990 K. This discrepancy This discrepancy likely arises because the LTE assumption equates electron and gas temperatures. Under this condition, rising temperature rapidly enhances ionization and electrical conductivity, leading to a positive feedback mechanism that sustains higher temperatures in a larger, more concentrated region near the coil. Under NLTE conditions, however, energy exchange between electrons and heavy particles is limited. Consequently, deposited electromagnetic energy cannot be efficiently transferred to the gas thermal energy. Combined with wall cooling, radial heat diffusion, and convective transport by the gas flow, this limitation reduces the peak temperature and shifts it downstream.

Furthermore, restricted electron-heavy particle energy transfer under NLTE conditions suppresses ionization, resulting in lower electron density and plasma conductivity than predicted by LTE. As a result, energy coupling efficiency decreases, and the high-temperature region becomes smaller compared to the LTE model.

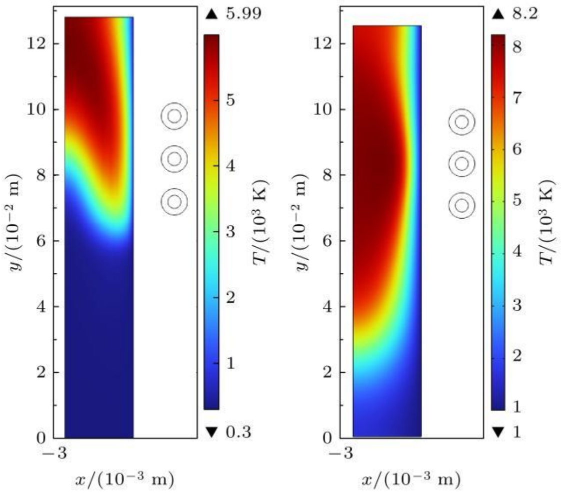

Fig. 3 Temperature cloud diagram of 1000 W non-equilibrium and equilibrium inductively coupled plasma discharge: (a) Non-equilibrium state; (b) equilibrium state.

Figure 4 presents the axial temperature distribution under LTE and NLTE models. The results indicate that the electron temperature in the NLTE model exceeds that of LTE near the induction coil, whereas it remains lower than LTE from the inlet to the upstream region of the coil. This occurs because the upstream electric field is relatively weak, resulting in limited Joule heating. In this region, electron-heavy particle collisional heat transfer dominates, driving the electron temperature toward the gas temperature. Additionally, the nonequilibrium model constrains ionization and electrical conductivity enhancement, thereby reducing local power deposition. In contrast, the LTE model, based on thermodynamic equilibrium assumptions, yields higher ionization degrees and electrical conductivity. Consequently, LTE sustains a certain level of heating even in weak electric field regions, leading to higher upstream temperatures compared to NLTE. Conversely, in the strong-field region near the coil, electrons are directly accelerated by the induced electromagnetic field by the induced field, forming a distinct electron temperature peak. However, LTE enforces equality between electron and gas temperatures, thereby suppressing the characteristic of preferential electron heating Thus, only near the coil does the NLTE electron temperature surpass that of LTE.

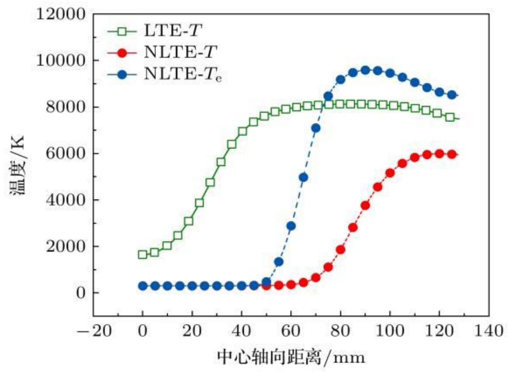

Fig. 4 Variation of temperature distribution along the central axis under the equilibrium model and the nonequilibrium model.

Results indicate that, in numerical simulations of inductively coupled plasmas (ICPs), accounting for non-equilibrium effects significantly influences predicted temperature fields. The non-local thermodynamic equilibrium (NLTE) model may more accurately capture the time lag in energy transfer and the flow-induced restructuring of temperature distribution. Therefore, the following analysis employs the NLTE model to examine the discharge process in detail, including electron heating mechanisms, energy transport characteristics, and the spatial disparity between electron and heavy-particle temperatures under non-equilibrium conditions. This approach further elucidates the physical properties and energy coupling mechanisms of ICPs within a non-equilibrium framework.

4.2 Numerical Simulation of Non-Equilibrium Inductively Coupled Plasma

Figure 5 illustrates the temporal evolution of gas temperature distribution within the generator under 1000 W power and argon inductively coupled discharge conditions.

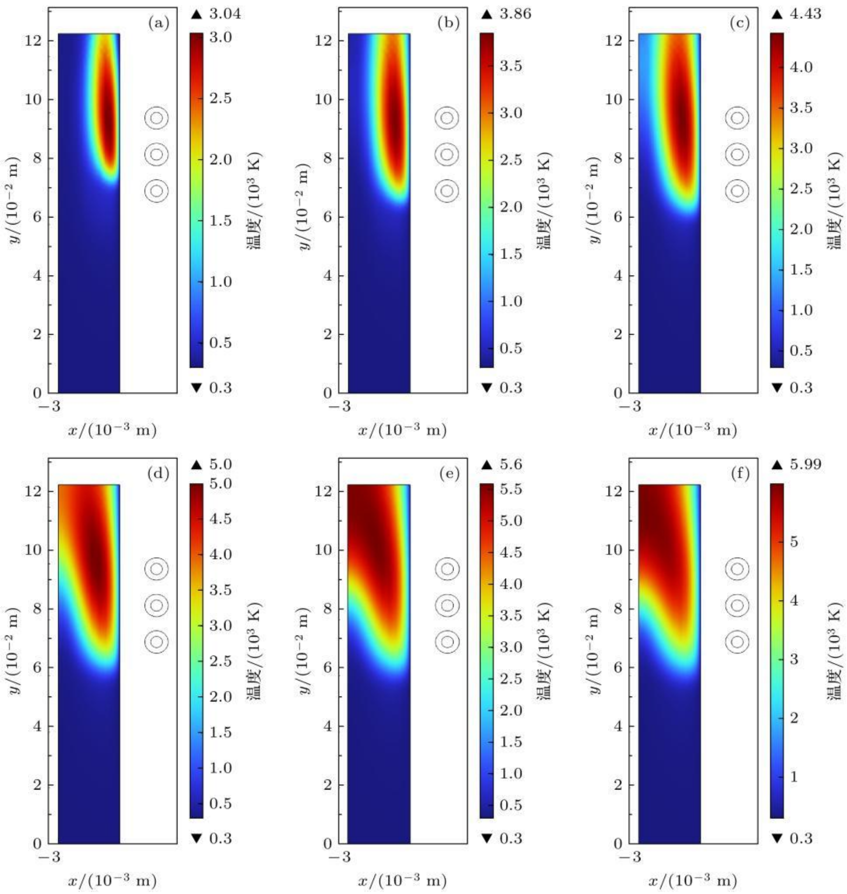

Fig. 5 The gas temperature distribution during the argon gas induction coupled plasma discharge process: (a) 2 ms; (b) 4 ms; (c) 6 ms; (d) 8 ms; (e) 9 ms; (f) 10 ms.

As shown in Figure 6, the electromagnetic field rapidly ignites the incoming argon gas, initiating discharge. The gas absorbs substantial Joule heating, significantly elevating the local temperature and establishing the primary plasma discharge region. This process produces a characteristic temperature distribution-high at the periphery and low at the center-thereby confirming the typical skin effect observed during inductively coupled plasma discharge.

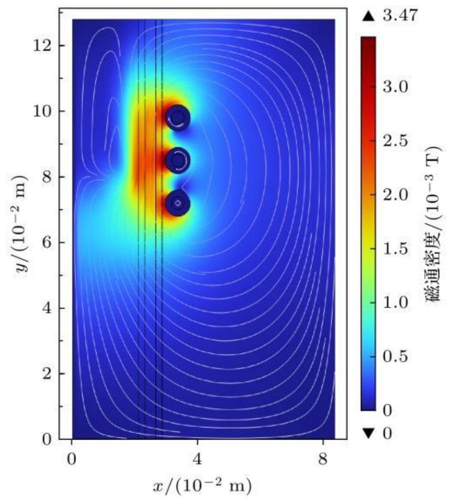

Fig. 6 Magnetic field distribution in the 1000 W discharge tube at the initial stage of discharge (2 ms).

Over time, the high-temperature region gradually expands. Under the combined effects of thermal conduction and convective heat transfer, it progressively extends toward the central axis and the outlet direction, as illustrated in Figure 7. Eventually, it stabilizes, forming a steady-state high-temperature discharge zone.

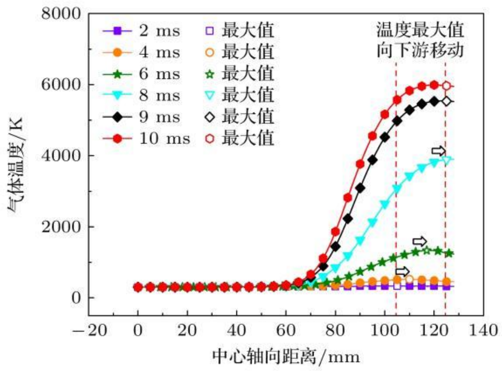

Fig. 7 The gas temperature distribution along the central axis at different times under 1000 W.

Figure 8 presents contour plots of plasma gas temperature and electron temperature at the same instant under identical operating conditions. The results indicate that the maximum gas temperature reaches 5990 K, whereas the peak electron temperature is 0.93 eV (1 eV ≈ 11605 K).

The gas temperature peak occurs in the downstream region of the plasma torch coil section, while the electron temperature peak is localized near the torch wall adjacent to the coil and remains consistently higher than the gas temperature. This discrepancy indicates that the plasma in this region is in a state of thermodynamic non-equilibrium. The phenomenon arises from the distinct heating mechanisms for electrons and gas in inductively coupled plasmas. The region near the coil experiences the strongest alternating magnetic field, where the induced electric field most effectively accelerates electrons, thereby sustaining elevated electron temperatures relative to other locations. Because electrons directly absorb electromagnetic field energy, their spatial temperature distribution is largely governed by the electric field profile and the skin effect, enabling a persistent electron temperature peak at the coil position.

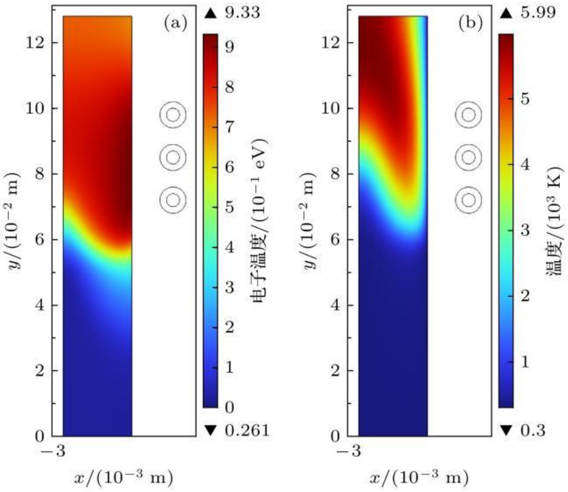

Fig. 8 Distribution cloud diagram of the 1000 W discharge tube during the steady-state phase: (a) Electron temperature; (b) gas temperature.

During the discharge maintenance phase, strong electron heating occurs near the coil. However, heat losses from wall cooling and radial thermal diffusion simultaneously reduce the collision frequency between electrons and heavy particles, limiting energy transfer. Consequently, the local gas temperature cannot remain elevated for extended durations, promoting the formation of a thermal non-equilibrium state between gas and electron temperatures near the coil wall. Moreover, gas flow within the plasma transports the heated gas downstream, shifting the peak gas temperature to a region downstream of the coil segment rather than to the coil location itself, where energy deposition is strongest. The gas velocity contour is shown in Figure 9.

Figure 10 presents the molar fraction distribution of species along the central axis of the discharge tube at 1000 W during the steady-state phase. The results indicate that ground-state argon (Ar) dominates the central axis, accounting for over 99% of the molar fraction, while the molar fractions of excited argon (Ar*) and argon ions (Ar^+) remain low. Additionally, along the central axis near the coil, the argon molar fraction decreases while the fractions of excited and ionized species increase. This phenomenon arises primarily because the high-frequency electromagnetic field concentrates in the coil region, efficiently accelerating electrons. This enhancement intensifies collisional excitation and ionization between electrons and ground-state argon atoms. As a result, significant particle state transitions occur along the central axis near the coil: ground-state argon undergoes excitation and ionization, reducing its molar fraction, while the fractions of excited and ionized species correspondingly rise.

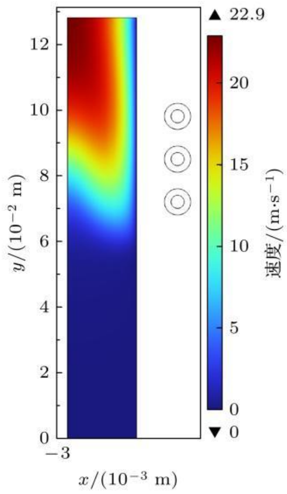

Fig. 9 Cloud diagram of gas velocity distribution in a 1000 W discharge tube during the steady-state stage.

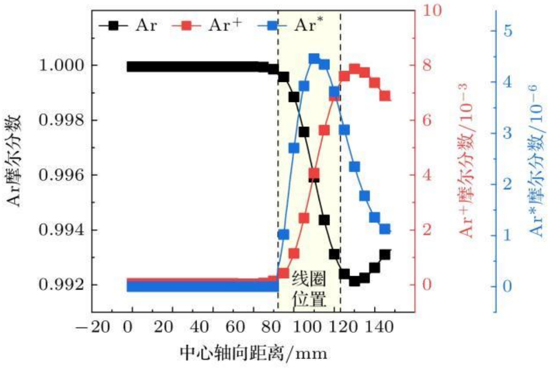

Fig. 10 The particle mole fraction distribution along the central axis of the 1000 W discharge tube during the steady-state stage.

The skin effect is a prominent phenomenon in high-frequency inductively coupled discharges. Skin depth provides a quantitative description of this effect. The formula for calculating skin depth is

$$\delta = \left(\frac{1}{\pi f \sigma_e \mu_0}\right)^{1/2} \quad (16)$$

σ_e denotes the electrical conductivity of the plasma; f represents the power supply frequency, and μ_0 is the magnetic permeability of the plasma, where $\mu_0 = 4\pi \times 10^{-7}$ H/m.

Based on calculations, the maximum gas temperature is approximately 6000 K, yielding an electrical conductivity of 147.093 S/m. At an operating frequency of 13.56 MHz, the skin depth formula gives a skin layer thickness of approximately 11.26 mm. Figure 11 illustrates the molar fraction distribution of species along the torch axis. The simulation reveals that Ar^+ reaches its peak molar fraction at r = 14 mm, while Ar* peaks at r = 19 mm-both positions lying within the skin layer. Excitation preferentially occurs in the near-wall region, where the electric field is strongest, leading to Ar* enrichment closer to the wall. In contrast, ions generated near the wall are rapidly dissipated by the sheath and wall surfaces, shifting the steady-state ion peak radially inward to a location where production and loss balance. These findings indicate that energy coupling in the discharge is dominated by the skin effect, and radial offsets arise between excitation and ionization/ion transport processes due to differences in energy thresholds, production-loss dynamics, and diffusion characteristics.

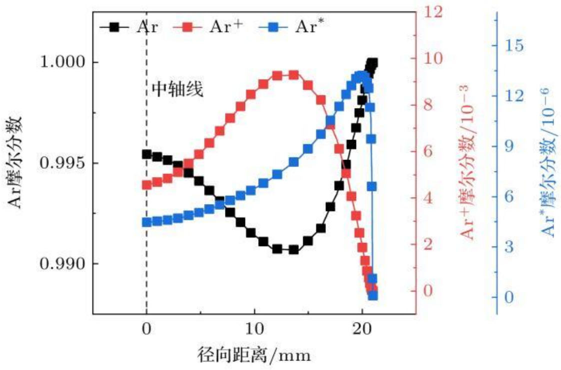

Fig. 11 The particle mole fraction distribution at the *z* = 91.5 mm cross-sectional plane (midway between coils 1 and 2) in the 1000 W discharge tube during the steady-state phase.

The molar fraction distribution of particles along the radial cross-section further indicates that energy coupling in the plasma discharge and particle transformation processes primarily occur within the skin layer adjacent to the coil. The central axis region remains dominated by ground-state particles due to weaker energy deposition. Additionally, near the wall, significant cooling from circulating water and thermal conduction losses cause rapid reductions in both plasma temperature and electron density. Consequently, the molar fractions of argon excited states and ions decrease sharply, leaving neutral atoms as the predominant species in this region.

We maintained all parameters constant except for the chamber pressure, which we set to 5 kPa and 10 kPa. Figure 12 presents the axial distributions of gas temperature and electron temperature under these two pressure conditions. As chamber pressure increases, the overall electron temperature within the ICP torch decreases. This trend primarily arises because higher pressure increases gas density, thereby shortening the electron mean free path. The resulting rise in collision frequency between electrons and heavy particles accelerates energy transfer-via both elastic and inelastic collisions-from electrons to surrounding particles, ultimately reducing electron temperature.

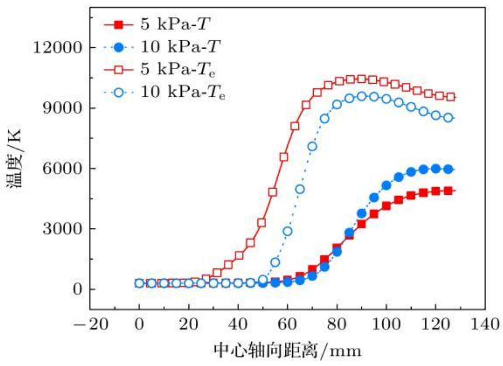

Fig. 12 The gas temperature and electron temperature along the centerline at different pressures.

In the upstream region (< 83 mm), electrons possess higher energy under lower pressure. Although collision frequency decreases, the reduced collision frequency limits overall energy transfer, resulting in more effective gas heating. Consequently, the gas temperature at 5 kPa exceeds that at 10 kPa. In the downstream region (> 83 mm), rapid expansion cooling in the low-pressure plasma reduces gas temperature. Conversely, elevated pressure enhances collision frequency between electrons and heavy particles, improving energy transfer efficiency and facilitating greater conversion of electron energy into gas internal energy, thereby further elevating gas temperature under high-pressure conditions.

As pressure decreases, Figure 12 illustrates an increasing disparity between electron and gas temperatures. This indicates that electrons retain higher energy under low pressure, while energy acquisition by heavy particles lags, leading to more pronounced thermal non-equilibrium characteristics.

5 Conclusions

1) At kPa-level pressures, the LTE and NLTE models yield significantly different predictions for the temperature field. The LTE assumption of equal electron and gas temperatures produces an unrealistically high temperature peak of 8200 K near the coil, with a large and concentrated high-temperature zone. In contrast, the NLTE model-accounting for limited energy exchange-predicts a maximum temperature of approximately 5990 K, with the peak shifted downstream and exhibiting the characteristic preferential electron heating non-equilibrium behavior. Thus, NLTE model provides a more physically realistic representation the true energy coupling mechanisms.

2) Analysis of the discharge process under the NLTE model reveals that discharge initiates near the coil wall, where the skin effect is pronounced. The high-temperature

region subsequently expands downstream and toward the central axis. The electron temperature peaks near the coil, whereas the gas temperature peaks further downstream, confirming a pronounced thermal non-equilibrium state state. Along the central axis, ground-state argon dominates; near the coil, fractions of excited and ionized species increase, indicating that the coil region serves as the core site for energy coupling and particle transformation.

3) Examination of axial distributions of gas and electron temperatures across varying pressures demonstrates that reduced pressure amplifies the temperature difference between electrons and gas, thereby intensifying thermal non-equilibrium characteristics.

Accurate experimental measurement of electron and gas temperatures in radio-frequency inductively coupled plasma (ICP) remains highly challenging due to its extremely high internal temperatures, spatial confinement, and strong coupling among electromagnetic fields and chemical reactions. To date, experimental investigations into thermal non-equilibrium characteristics of ICP at kPa-level pressures remain scarce. Existing studies indicate that spectral fitting based on the local thermodynamic equilibrium (LTE) assumption in non-equilibrium regions may underestimate electron temperature, necessitating diagnostic approaches that explicitly account for non-equilibrium effects. Yu et al.[25] developed an NLTE model at kPa-level pressures and compared it with experimental spectral measurements by Satoshi et al.[26], finding good agreement between the model-predicted translational temperature and experimental data. Although that study employed nitrogen as the working gas, its energy transfer mechanism-wherein electrons absorb radio-frequency energy and subsequently relax energy to heavy particles-is identical to that in argon ICP. Therefore, this work provides critical experimental validation for the reliability of the NLTE model adopted in the present study under kPa-level pressure conditions.

References

[1] Zhan Z H, Wang C H, Zhou Q J, Liu C Z, Zhao P 2022 *Trans. China Electrotech. Soc.* **37** 2725

[2] Bottin A, Carbonaro M, Haegen V V, Paris S 1999 *ESA Publications Division* **462** 553

[3] Panerai F, Chazot O 2012 *Mater. Chem. Phys.* **134** 597

[4] Ito T, Ishida K, Mizuno M, Sumi T, Matsuzaki T, Nagai J, Murata H 2005 *43rd AIAA Aerospace Science Meeting and Exhibit* Reno, Nevada, January 10−13, 2005 pp10−13

[5] Lin L, Wu B, Wu C K 2001 *Acta Aerodyn. Sin.* **19** 407

[6] Liu L P, Wang G L, Wang Y G, Zhang J, Luo L 2017 *Acta Aeronaut. Astronaut. Sin.* **39** 421696

[7] Luo L, Wang Y, Liu L, Duan L, Wang G, Lu Y 2016 *Carbon* **103** 73

[8] Zhang X N, Li H P, Murphy A B, Xia W D 2013 *High Volt. Eng.* **39** 1640

[9] Fujino T, Ito S, Okuno Y 2021 *IEEE Trans. Plasma Sci.* **49** 2954

[10] Al-Mamun S A, Tanaka Y, Uesugi Y 2010 *Plasma Chem. Plasma Process.* **30** 141

[11] Fujita K, Suzuki T, Mizuno M, Fujii K 2009 *J. Thermophys. Heat Transf.* **23** 840

[12] Tanaka Y, Sakuta T 2002 *J. Phys. D: Appl. Phys.* **35** 2149

[13] Degrez G, Abeele D V, Barbante P, Bottin B 2004 *Int. J. Numer. Methods Heat Fluid Flow* **14** 538

[14] Li R Z, Ni G H, Sun H M, Wang C 2024 *Chin. J. Vac. Sci. Technol.* **44** 819

[15] Liu Y, Xia G 2025 *6th International Conference on Mechatronics Technology and Intelligent Manufacturing* Nanjing, China, April 11−13, 2025 pp226−229

[16] Zhang Y H, Zhao X Q, Liang Y S, Guo Y Y 2024 Acta Phys. Sin. **73** 135201 Yu H Z, Xin Q Z, Ying S L, Yuan Y G 2024 *Acta Phys. Sin.* **73** 135201

[17] Stewart R A, Vitello P, Graves D B 1994 *J. Vac. Sci. Technol. B* **12** 478

[18] Lei F, Li X, Liu Y, Liu D, Yang M, Yu Y 2018 *AIP Adv.* **8** 015003

[19] Punjabi S B, Joshi N K, Mangalvedekar H A, Lande B K, Das A K, Kothari D C 2012 *Phys. Plasmas* **19** 012108

[20] Zhu H L, Tong H H, Yang F Z, Cheng C M, Ye G Y 2013 *High Volt. Eng.* **39** 1621

[21] Yu D P, Wu J, Tu J, Zhang S Y, Xin Q, Wan Y J 2020 *J. Harbin Inst. Technol.* **52** 82

[22] Fujita K, Suzuki T, Ozawa T 2011 *27th International Symposium on Rarefied Gas Dynamics* Pacific Grove, California, USA, July 10−15, 2011 pp407−412

[23] Xu Z, Gong X Y, Du D, Chen W B 2018 *J. Low Temp. Phys.* **40** 36

[24] 2025-08-25 [Rong Mingzhe http://plasma-data.net/index [2025-08-25

[25] Yu M, Yamada K, Takahashi Y, Liu K, Zhao T 2016 *Phys. Plasmas* **23** 123523

[26] Satoshi M, Kazuhiko Y, Takashi A 2015 *JAXA Special Publication* JAXA-SP-**14**-010 17−22